



Introduction of Prognostic Graupel Density in Weather Research and Forecasting (WRF) Double-Moment 6-Class (WDM6) Microphysics and Evaluation of the Modified Scheme During the ICE-POP Field Campaign

Sun-Young Park¹, Kyo-Sun Sunny Lim¹, Kwonil Kim², Gyuwon Lee¹, and Jason A. Milbrandt³

5 ¹Department of Atmospheric Sciences, Center for Atmospheric Remote Sensing (CARE), Kyungpook National University, Daegu, Republic of Korea

²School of Marine and Atmospheric Sciences, Stony Brook University, NY, United States

³Environment and Climate Change Canada, Atmospheric Numerical Weather Prediction Research, Dorval, QC, Canada

Correspondence to: Kyo-Sun Sunny Lim (kyosunlim@knu.ac.kr)



Abstract

The Weather Research and Forecasting (WRF) Double-Moment 6-class (WDM6) scheme was modified by incorporating prognostic graupel density. Explicitly prognosed graupel density, in turn, modifies graupel characteristics such as the fall velocity–diameter and mass–diameter relationships of graupel. The modified WDM6 has been evaluated based on a two-dimensional (2D) idealized squall line simulation and winter snowfall events that occurred during the International Collaborative Experiment for Pyeongchang Olympics and Paralympics (ICE-POP 2018) field campaign over the Korean Peninsula. From the 2D simulation, we confirmed that the modified WDM6 can simulate varying graupel density, ranging from low values in an anvil clouds region to high values in the convective region at the mature stage of a squall line. Simulations with the modified WDM6 increase graupel amounts at the surface and decreased graupel aloft because of the faster sedimentation of graupel for two winter snowfall cases during the ICE-POP 2018 campaign, as simulated in the 2D idealized model. The altered graupel sedimentation in the modified WDM6 influenced the magnitude of the major microphysical processes of graupel and snow, subsequently reducing the surface snow amount and precipitation over the mountainous region. The reduced surface precipitation over the mountainous region mitigates the surface precipitation bias observed in the original WDM6, resulting in better statistical skill scores for the root mean square errors. Notably, the modified WDM6 reasonably captures the relationship between graupel density and its fall velocity, as retrieved from 2D video disdrometer measurements, thus emphasizing the necessity of including prognostic graupel density to realistically represent the microphysical properties of graupel in models.

1. Introduction

Over the past decades, the parameterization of ice microphysics traditionally represents ice-phase particles as pre-defined categories of solid-phase hydrometeors in bulk-type cloud microphysics (Lin et al., 1983; Rutledge and Hobbs, 1983; Cotton et al., 1986; Ferrier 1994; Meyers et al., 1997; Thompson et al., 2004; Hong and Lim, 2006; Seifert and Beheng, 2006; Morrison et al., 2009), bin-type cloud microphysics schemes (Reisin et al., 1996; Geresdi 1998; Khain et al., 2004; Lebo and Seinfeld, 2011) and Lagrangian "Super particle" microphysics schemes (Grabowski et al., 2019; Morrison et al., 2020; Shima et al., 2020). Solid-phase hydrometeors in cloud microphysics schemes are classified into typical particle types, such as ice crystals, aggregates, graupel and hail. Each category of hydrometeors is characterized by static parameters defining density, diameter–mass relationship and diameter–fall velocity relationship, which are expressed differently in each microphysics scheme. Several studies reported that the simulated convections were considerably sensitive to the manner of categorization of solid-phase hydrometeors (Gilmore et al., 2004; Cohen and McCaul, 2006; Morrison and Milbrandt, 2011; Bryan and Morrison, 2012; Adams-Selin et al., 2013). Gilmore et al. (2004) and Cohen and McCaul (2006) reported that when simulating supercell storms, the simulated precipitation varies considerably according to the static parameters defining hail/graupel characteristics. Morrison and Milbrandt (2011) demonstrated that different approaches in treating graupel or hail produce



distinct differences in storm structure, precipitation, and cold pools strength for idealized supercells. Bryan and Morrison (2012) showed that the fall velocities of graupel and hail affect the simulated reflectivity and dynamics for an idealized squall line. Adams-Selin et al. (2013) reported that the development of a bow echo is highly sensitive to the parameters defining the
45 fall velocities of graupel and hail.

Since the study of Wisner et al. (1972), research on microphysics schemes has focused on augmenting the parameterisation of cold rain processes by increasing the number of solid-phase categories or introducing new prognostic variables for these categories (Cotton et al., 1986; Ferrier 1994; Reisner et al., 1998; Milbrandt and Yau, 2005; Bae et al., 2019). More recently, modelling approaches have evolved toward ways of predicting solid-phase characteristics or considering
50 various shapes of ice crystals (Morrison and Grabowski, 2008; Mansell et al., 2010; Milbrandt and Morrison, 2013; Morrison and Milbrandt, 2015; Jensen et al., 2017; Tsai and Chen, 2020; Jensen et al., 2023). Morrison and Grabowski (2008) devised a new method that allows the changing mass–dimension and projected-area–dimension relationships of ice particles to evolve according to the predicted rime mass fraction and particle dimension. Mansell et al. (2010) and Milbrandt and Morrison (2013, hereafter MM13) implemented a new approach of incorporating a prognostic graupel density. By advancing the study of MM13,
55 Morrison and Milbrandt (2015) later developed the Predicted Particle Properties (P3) bulk microphysics scheme that predicts the rime mass fraction, rime volume, and predicted rime density for a single generic ice-phase category. Meanwhile, Jensen et al. (2017) introduced the Ice-Spheroids Habit Model with Aspect-ratio Evolution (ISHMAEL) bulk microphysics scheme, which predicts the evolution of the ice-particle aspect ratio for two ice species, namely, planar-nucleated (ice-one) and columnar-nucleated (ice-two) particles. Chen and Tsai (2020) proposed a bulk-type microphysics scheme that allows variations
60 in the shape and density of solid-phase hydrometeors. Recently, Jensen et al. (2023) implemented a prognosed density graupel category into the Thompson–Eidhammer scheme (Thompson and Eidhammer, 2014), following the approach of Mansell et al. (2010) and MM13.

Various studies demonstrated the merits of considering the prognostic density of solid-phase hydrometeors when simulating convective storms (Dawson et al., 2014; Johnson et al., 2016; Labriola et al., 2017; Jouan and Milbrandt, 2019)
65 Dawson et al. (2014) demonstrated that the reflectivity of a simulated supercell depends strongly on the characteristics of the graupel/hail in the microphysics scheme. Specifically, variations in the fall velocity and density of graupel/hail have a profound effect on reflectivity signatures. Johnson et al. (2016) evaluated the reproducibility of the polarisation signatures in supercell storms for several partially or fully two-moment (2M) schemes. Realistic signatures were obtained only with those microphysics schemes that predicted graupel density. Labriola et al. (2017) performed supercell thunderstorm simulations and
70 demonstrated that the inclusion of low-density graupel in a 2M scheme facilitated the reduction of reflectivity. They further showed that by predicting the density of graupel/hail in a 2M scheme, a spectrum of rime ice characteristics can be obtained. Jouan and Milbrandt (2019) demonstrated that variations in the simulated storm reflectivity and precipitation structure exhibit more pronounced differences when using predicted particle density instead of a fixed particle density in the 2M scheme, particularly related to different number concentrations of cloud condensation nuclei in a mid-latitude continental squall line.



75 Based on their analysis, they suggested that an accurate representation of graupel in microphysics schemes is crucial for appropriately simulating the effects of changes in the concentration of cloud condensation nuclei in selected systems.

The Weather Research and Forecasting (WRF) Double-Moment 6-class (WDM6) scheme (Lim and Hong, 2010), a bulk-type microphysics scheme, has been widely evaluated for predicting deep convective precipitation in summer season (Min et al., 2015; Song and Sohn, 2018; Kim et al., 2022) and snowfall events in winter season (Liu et al., 2011; McMillen and Steenburgh, 2015; Morrison et al., 2015; Comin et al., 2018; Lim et al., 2020; Ko et al., 2022). Several studies showed that the WDM6 scheme produces excess graupel compared to other microphysics schemes during the summer and winter seasons. Li et al. (2019) showed that the simulated precipitation exhibits significant sensitivity to changes in graupel density in the WDM6 scheme. Recognizing the sensitivity and importance of the representation of graupel to simulate precipitation, we introduced a new prognostic variable, the graupel volume mixing ratio, to predict graupel density based on the study of MM13. The impact of the modified WDM6 scheme on the simulated convections was evaluated through a two-dimensional (2D) idealized squall line experiment and by considering snowfall events that occurred during the International Collaborative Experiment for Pyeongchang Olympics and Paralympics (ICE-POP 2018) field campaigns over the Korean Peninsula. The novelty of our study lies in comparing the simulated graupel characteristics in the WDM6 scheme with the specialized observed data during ICE-POP 2018.

90 The remainder of this paper is organized as follows. Section 2 explains the implemented method of the new prognostic variable, namely, the graupel density. The experimental setups, including the case description, model setup and observations for verification, are described in Section 3. The results and a summary are provided in sections 4 and 5, respectively.

2. New prognostic variable (graupel density) in the WDM6 scheme

95

In the original WDM6 scheme, graupel characteristics are pre-defined using the static value of density (ρ_G), constant coefficients for the mass (M_G)–diameter (D_G) and fall velocity (V_G)– D_G relationships. This study introduces a prognostic variable, namely, the volume mixing ratio (B_G). B_G varies dynamically in both time and space, reflecting the formation and growth mechanisms of graupel. The conservation equation for B_G is given by

$$100 \quad \frac{\partial B_G}{\partial t} = -\vec{V} \cdot \nabla_3 B_G - \frac{1}{\rho_a} \frac{\partial}{\partial z} (\rho_a B_G V_{B_G}) + S_{B_G}, \quad (1)$$

The first, second and third terms on the right-hand side of Eq. (1) represent the 3D advection, sedimentation of B_G and sources and sinks of B_G (S_{B_G}). \vec{V} and V_{B_G} represent the three-dimensional 3D wind fields and the B_G -weighted mean terminal velocities of graupel, respectively; ρ_a is the air density. S_{B_G} comprise several microphysical source/sink processes q_G and density of specific hydrometeors (ρ_X) according to Eq. (2). The meanings of the microphysical processes in Eq. (2) are summarized in Table 1, and their detailed descriptions are available in the literature (Appendix B of Park and Lim, 2023). The rain density (ρ_R) is set as 1000 kg m^{-3} ; the cloud ice density (ρ_I) and snow density (ρ_S) are taken as 500 and 100 kg m^{-3} , respectively. Meanwhile, ρ_G can be prognosed once q_G and B_G are updated using Eq. (3).

105



$$S_{BG} = \begin{cases} \frac{Piacr}{\rho_R} + \frac{Praci}{\rho_I} + \frac{Pracs}{\rho_S} + \frac{Psacr}{\rho_R} + \frac{Pgaci}{\rho_I} + \frac{Pgacw}{\rho_R} + \frac{Psacw}{\rho_R} + \frac{Pgacr}{\rho_R} + \frac{Pgdep}{\rho_G} + \frac{Pgfrz}{\rho_R} & (T < T_0) \\ \frac{Pgmlt}{\rho_G} + \frac{Pgeml}{\rho_G} + \frac{Pg evp}{\rho_G} & (T \geq T_0) \end{cases} \quad (2)$$

$$\rho_G = \frac{q_G}{B_G} \quad (3)$$

110

Table 1. Meanings of the microphysical source/sink processes in Eq. 2.

Symbol	Meaning	SI unit
Paacw	Production rate for accretion of cloud water by snow or graupel	kg kg ⁻¹ s ⁻¹
Pgaci	Production rate for accretion of cloud ice by graupel	kg kg ⁻¹ s ⁻¹
Pgacr	Production rate for accretion of rain by graupel	kg kg ⁻¹ s ⁻¹
Pgacw	Production rate for accretion of cloud water by graupel	kg kg ⁻¹ s ⁻¹
Pgdep (Pgsub)	Production rate for deposition (sublimation) rate graupel	kg kg ⁻¹ s ⁻¹
Pgeml	Production rate induced by enhanced melting of graupel	kg kg ⁻¹ s ⁻¹
Pgevp	Production rate for evaporation of melting graupel	kg kg ⁻¹ s ⁻¹
Pgfrz	Production rate for freezing of rainwater to graupel	kg kg ⁻¹ s ⁻¹
Pgmlt	Production rate for melting of graupel to form rain	kg kg ⁻¹ s ⁻¹
Piacr	Production rate for accretion of rain by cloud ice (graupel)	kg kg ⁻¹ s ⁻¹
Praci	Production rate for accretion of cloud ice (graupel) by rain	kg kg ⁻¹ s ⁻¹
Pracs	Production rate for accretion of snow by rain	kg kg ⁻¹ s ⁻¹
Psacr	Production rate for accretion of rain by snow	kg kg ⁻¹ s ⁻¹



Psacw

Production rate for accretion of cloud water by snow

kg kg⁻¹ s⁻¹

The M_G – D_G relationship can be expressed as $M_G(D_G) = c_G D_G^{d_G}$. Here, c_G and d_G are set as $\frac{\pi \rho_G}{6}$ and 3.0, respectively, because the graupel is assumed to be a sphere in the original WDM6 scheme. Further, c_G is treated as a constant since ρ_G is set as a constant (500 kg m⁻³). In our modified WDM6, c_G varies with the prognosed ρ_G (Eq. (3)). Meanwhile, the Reynolds number (Re)–Best number (X) relationship produces the power-law expressions of fall velocity across four categories of ice particles based on the relationships of mass and projected area with the dimensions (Mitchell 1996) as Eq. (5). The Re–X relationship was further refined by Khvorostyanov and Curry (2002) to derive the continuous power law of ice-particle dimension by adopting varying drag terms (a_1 and b_1) (Eqs. (6) and (7)).

$$120 \quad Re = a_1 X^{b_1}, \quad (5)$$

$$a_1 = \frac{c_2 [(1 + c_1 X^{1/2})^{1/2} - 1]^2}{X}, \quad (6)$$

$$b_1 = \frac{c_1 X^{1/2}}{2 [(1 + c_1 X^{1/2})^{1/2} - 1] (1 + c_1 X^{1/2})^{1/2}}. \quad (7)$$

The non-dimensional surface roughness parameters, namely C_1 , C_2 , δ_0 and C_0 , in Eqs. (6) and (7) are assumed as $4/(\delta_0^2 C_0^2)$, $\delta_0^2/4$, 5.83 and 0.6, respectively. The Best number, X, is expressed as a function of ρ_G shown in Eq. (8).

$$125 \quad X = \frac{4 \rho_G g \rho_a D_{GM}^3}{3 \eta^2}, \quad (8)$$

where g is the acceleration due to gravity, and η represents the dynamic viscosity. D_{GM} is the maximum dimension of the graupel. Eq. (9) represents the V_G – D_G relationship. Here, a_G and b_G are derived from the study of Mitchell and Heymsfield (2005). By assuming the shape of graupel as a sphere, a_G and b_G can be expressed as shown in Eqs. (10) and (11).

$$V_G = a_G D_G^{b_G}, \quad (9)$$

$$130 \quad a_G = a_1 v^{(1-2b_1)} \left(\frac{2 c_G g}{\rho_a \gamma} \right)^{b_1}, \quad (10)$$

$$b_G = b_1 (c_G - \sigma + 2) - 1, \quad (11)$$

where v is the kinematic viscosity of air. Further, c_G and d_G represent the coefficients of the M_G – D_G relationship, while γ and σ are the coefficients of the area (A_G)– D_G relationship, $A_G = \gamma D_G^\sigma$, and they are set as $\frac{\pi}{4}$ and 2.0, respectively. These four coefficients vary depending on ice-particle types. Note that a_1 and b_1 can be obtained from Eqs. (6) and (7).

135 The density of graupel in the modified WDM6 scheme is assigned in the range of 100–900 kg m⁻³ at intervals of 100 kg m⁻³ to facilitate transition between aggregate and rime particles (Straka and Mansell, 2005). Further, a_G and b_G in the V_G – D_G relationship are derived at the given ρ_G using the least-squares method in a log–log space over a range of D_G of 0.3–20 mm (Table 2). Note that the coefficients, a_G and b_G , are assumed as 330 m^{1-b} s⁻¹ and 0.8 in the original WDM6 scheme. Figure 1

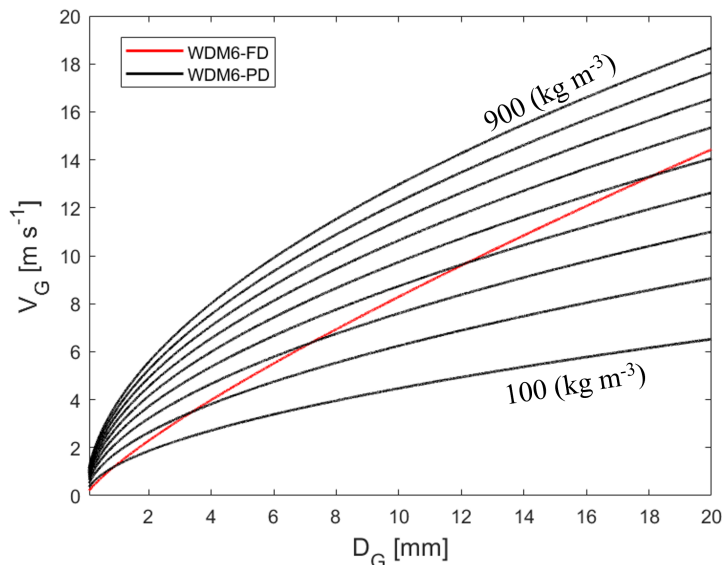


140 shows the retrieved V_G – D_G relationship in the modified WDM6 with ρ_G varying from 100 to 900 kg m⁻³. The newly retrieved
relationship can represent the wide range of V_G with varying ρ_G and D_G , unlike the relationship in the original WDM6. The
145 modified scheme is an extension of the WDM6 scheme, and it is incorporated with the prognostic cloud ice number
concentration (Park and Lim, 2023).

Table 2. Fitted parameters of a_G and b_G in the graupel fall velocity (V_G)–diameter (D_G) relationship with varying graupel density (ρ_G) (Eq. 9).

ρ_G (kg m ⁻³)	a_G (m ^{1-b} s ⁻¹)	b_G
100	54.9153	0.5446
200	74.2262	0.5375
300	88.8313	0.5339
400	101.0411	0.5316
500	111.7359	0.5299
600	121.3625	0.5286
700	130.1841	0.5275
800	138.3714	0.5266
900	146.0422	0.5258

Figure 1: V_G (m s⁻¹) as a function of D_G (mm) with various ρ_G between 100 and 900 (kg m⁻³), utilizing a_G and b_G values from Table 1. The V_G – D_G relationship in the original WDM6 scheme (WDM6_FD) is shown by a red line.



150 3. Experimental setup

3.1 Case description and model setup

3.1.1 Two-dimensional idealized squall line

155

The experimental design for the 2D idealized squall line simulation follows that of the study conducted by Lim and Hong (2010). A warm bubble with a 4 km radius and a maximum perturbation of 3 K at the centre of the domain drives the convection. A wind of 12 m s^{-1} is applied in the positive x direction at the surface, and it decreases to zero at a height of 2.5 km above the ground; there is no wind above this level. Additionally, no Coriolis force or friction is added, and an open boundary condition is applied for the simulation. By using the fixed initial conditions and considering only cloud microphysics parameterisation as the physical option, the impact of prognostic density on the simulated squall line can be distinguished and identified. The grid in the x direction comprises 601 points with a grid spacing of 1 km, and 80 vertical layers are configured. The model integration duration is 6 h with a time step of 5 s.

160

165 3.1.2 Snowfall during the ICE-POP field campaign

Eight snowfall events were observed during the ICE-POP field campaign period. These events can be classified into three categories (cold low, CL; warm low, WL; and air–sea interaction) according to the synoptic characteristics (Jeoung et al., 2020). Ko et al. (2022) used these eight events to compare the performances of various bulk-type microphysics schemes



170 in simulating snowfall events. In this study, we also selected eight identical cases, following Ko et al. (2022). Table 3 lists the
 model forecast and analysis periods, synoptic features and observed accumulated precipitation (mm) for each simulation case
 during the analysis period. For an in-depth analysis, we selected cases 1 and 2 as the representative examples for the CL and
 WL categories because these two cases exhibit the most representative features of precipitation distribution for each category.
 However, no case was selected for the air–sea interaction category because only one event from this category was identified
 175 during the ICE-POP field campaign. Further details regarding the characteristics of each category are provided in literature
 (Jeoung et al., 2020; Kim et al., 2021).

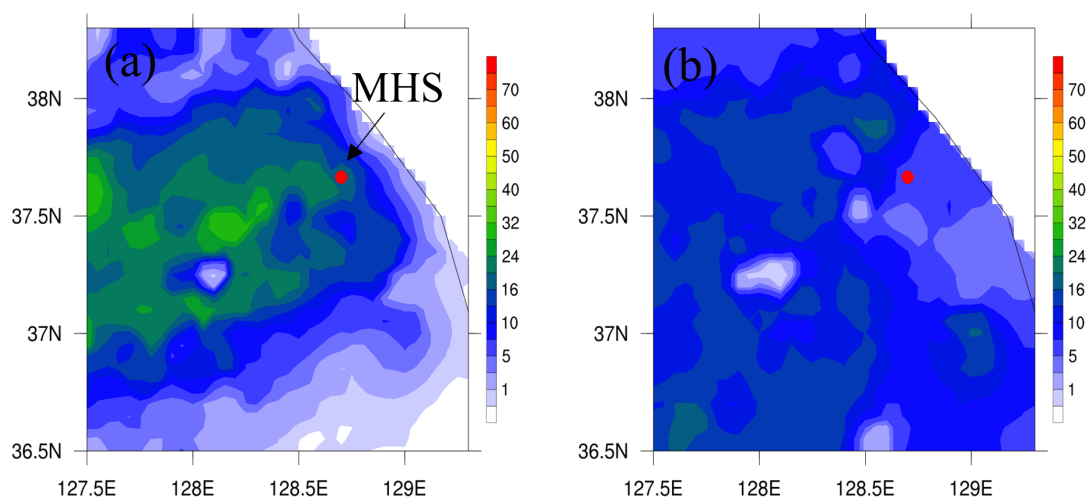
180 **Table 3. Forecast and analysis periods of the selected snowfall events during International Collaborative Experiment for
 Pyeongchang Olympics and Paralympics (ICE-POP 2018) field campaign. The observed precipitation (mm) during the analysis
 period, obtained from the automatic weather station (AWS) by the Korea Meteorological Administration (KMA), and the synoptic
 features of the cases, addressed in previous studies (Jeoung et al., 2020; Ko et al., 2022) are noted.**

Case	Forecast Period (UTC)	Analysis period (UTC)	Synoptic Feature	Observed precipitation (mm)
Case1	11.24.2017. 12:00 ~ 11.26.2017. 12:00	11.24.2017. 20:00 ~ 11.26.2017. 00:00	Cold Low	32.09
Case2	12.23.2017. 12:00 ~ 12.24.2017. 18:00	12.23.2017. 20:00 ~ 12.24.2017. 12:00	Warm Low	18.6
Case3	01.22.2018. 00:00 ~ 01.23.2018. 06:00	01.22.2018. 03:00 ~ 01.23.2018. 00:00	Cold Low	6.03
Case4	02.27.2018. 18:00 ~ 03.01.2018. 00:00	02.27.2018. 23:00 ~ 02.28.2018. 18:00	Warm Low	57.12
Case5	03.04.2018. 00:00 ~ 03.05.2018. 12:00	03.04.2018. 08:00 ~ 03.05.2018. 09:00	Warm Low	55.17
Case6	03.07.2018. 00:00 ~ 03.08.2018. 12:00	03.07.2018. 05:00 ~ 03.08.2018. 10:00	Warm Low	33.07
Case7	03.15.2018. 00:00 ~ 03.16.2018. 00:00	03.15.2018. 08:00 ~ 03.15.2018. 18:00	Air–sea interaction	25.52
Case8	03.20.2018. 12:00 ~ 03.21.2018. 18:00	03.20.2018. 18:00 ~ 03.21.2018. 14:00	Warm Low	25.83



185 Figure 2 shows the accumulated precipitation amount (mm) obtained from a heated tipping rain gauge at automatic
weather station (AWS). The dot in Fig. 2 indicates the location of the MHS (MayHills Supersite; 37.6632°N, 128.6996°E, 289
m mean sea level, MSL), where observation data from a 2D video disdrometer (2DVD) were collected to verify the model
simulation results. These data will be explained in Section 3.2 together with the AWS data. In the CL case, the low-pressure
region is located to the north of the polar jet stream and crosses over the middle of the Korean Peninsula, leading to significant
precipitation in the that region (Fig. 2a). Meanwhile, in the WL case, the low pressure is positioned to the south of the polar
jet stream and crosses over the southern part of the Korean Peninsula, heading towards the southeast and resulting in abundant
190 precipitation in the coastal region in the WL case (Fig. 2b).

Figure 2: Accumulated precipitation amount (mm) during the analysis period, obtained from AWS observation for (a) CL and (b) WL cases. The location of the observation site over the mountain, MayHills Supersite (MHS), is marked as a red dot.



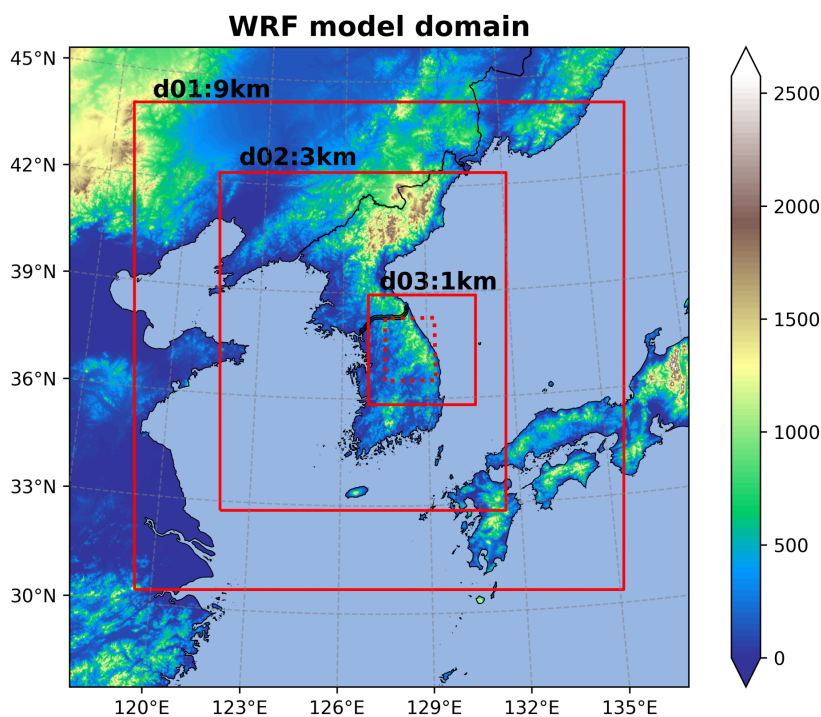
195 The winter snowfall simulations during the ICE-POP 2018 field campaign were conducted using three nested domains
(Fig. 3) with a horizontal grid spacing of 9, 3 and 1 km consisting of 170×170 , 295×349 and 331×340 grid points,
respectively. The model integration applies a one-way nesting. The top layer for the model is placed at 50 hPa, with a total of
65 vertical levels. Different integration time steps are used for each domain: 45 s for D01, 15 s for D02 and 5 s for D03. The
ERA–Interim reanalysis data are used from the European Centre for Medium-Range Weather Forecasts (ECMWF) for the
200 initial and boundary conditions (Dee et al., 2011a). For physics parameterisation, the Kain–Fritsch cumulus parameterisation
scheme (Kain, 2004) is used and applied only to the outer grid (9 km). The Revised MM5 Monin–Obukhov surface layer
(Jiménez et al., 2012) and the Rapid Radiative Transfer Model for General Circulation Models (RRTMG) long- and short-



205

wave radiative schemes (Iacono et al., 2008) are used. For planetary boundary layer schemes and land surface models, Yonsei University (YSU) (Hong et al., 2006) and Noah Multi-Parameterisation (Noah-MP) models (Chen and Dudhia, 2001) are used.

Figure 3: Three nested-model domains with horizontal resolutions of 9, 3 and 1 km with the terrain height (m) (shaded). The dashed box denotes the analysis domain.



210 3.2 Numerical experiments and observation data for verification

The WRF version 4.1.3 (Skamarock et al., 2008) is used to simulate the 2D-idealized squall line and the wintertime snowfall cases during the ICE-POP 2018 field campaign. Two experiments, named, WDM6_FD and WDM6_PD, are conducted for each case to examine the impact of the prognostic graupel density on the simulated convections. WDM6_FD uses the original WDM6 scheme with a fixed density (FD) (Lim and Hong, 2010; Park and Lim, 2023), and WDM6_PD uses the modified WDM6 scheme with prognostic density (PD).

To evaluate the simulated precipitation, AWS data, from stations operated by the Korea Meteorological Administration (KMA), are used. South Korea has a total of 604 AWS surface sites. To match the horizontal resolution of the AWS, we interpolate the 1 km model simulation results to 5 km grid. Additionally, we used the 2DVD measured data of the



220 diameter, fall velocity and geometry of each hydrometeor falling into a sampling area of 100 cm² to validate whether the model
effectively reproduces the observation-derived density–fall velocity relationship of graupel. Particle fall velocity was directly
measured by the 2DVD, but particle density was estimated based on the study of Huang et al. (2015), who adopted the Böhm
method (Böhm, 1989) using the observed geometry and the 2DVD fall velocity. This method leverages the capability of the
2DVD to measure individual particles using two orthogonal cameras, making it possible to reliably estimate particle geometry,
225 fall velocity and density. To ensure accurate measurement of the fall velocity, any instances when the collocated anemometer
recorded 1-min wind speeds exceeding 3.0 m s⁻¹ were excluded from the analysis.

Relying solely on the 2DVD-based particle characteristics makes it challenging to differentiate graupel from other
hydrometeors because of the unproven pre-defined assumptions on the shape, diameter and fall velocity of graupel particles
in developing a hydrometeor classification algorithm. Therefore, in addition we used a collocated multi-angle snowflake
230 camera (MASC), which captures pictures of each hydrometeor at three different angles, offering significant advantages in
identifying the degree of riming and habit classification. The MASC can provide the riming index (0–1) and the complexity
of the particle, which decreases as a particle becomes more spherical. These two parameters are obtained using the hydrometeor
classification algorithm (Praz et al., 2017), which determines the riming index by using a pre-trained supervised machine
learning model and the computed geometric parameters of each particle. To identify the graupel-dominant period, the following
235 stringent criteria are considered. The 10-min median riming index should be 1, and the 10 min median complexity of the
particles should be less than 1.35. Using our criteria, we identified 11,995 graupel particles over an accumulated period of 81
min in Case 6 (Table 3).

240 4. Results

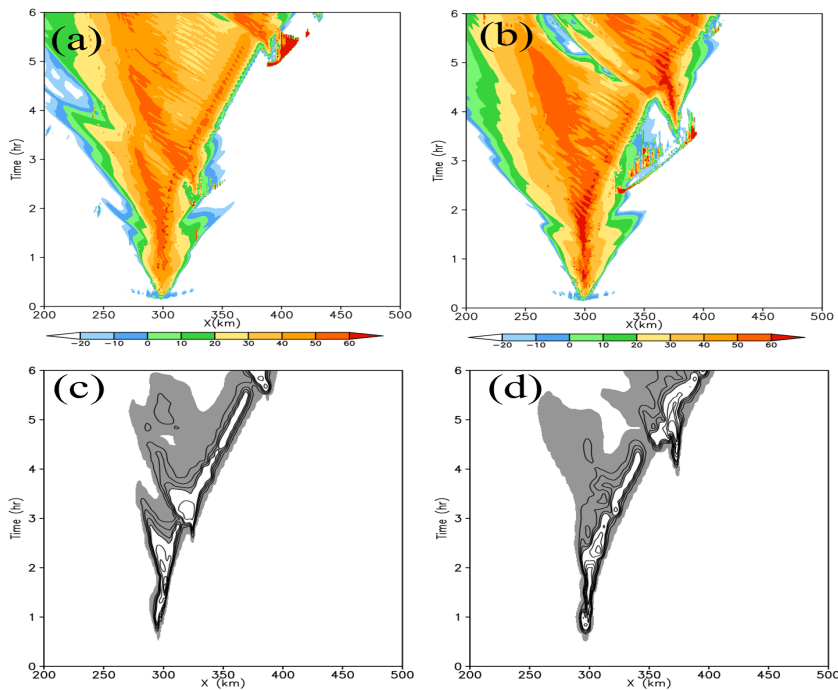
4.1 Two-dimensional idealized squall line experiment

The Hovmöller plots of the maximum reflectivity and surface rainfall rate for WDM6_FD and WDM6_PD
illustrate the typical evolution of a storm associated with squall line development (Fig. 4). The reflectivity is calculated
245 using a simulated equivalent reflectivity factor, which is defined as the sixth moment of the particle size distribution
based on the available mixing ratios and number concentrations for precipitation species including rain, snow and
graupel. Both WDM6_FD and WDM6_PD simulate the strong reflectivity along the convective core region and the
trailing weak reflectivity over the stratiform region, which is the general feature of squall lines (Figs. 4a and 4b).
WDM6_PD simulates a stronger reflectivity over both, convective and stratiform regions, but compared to
250 WDM6_FD, WDM6_PD simulates lower precipitation activities along the leading edge of the convection before 4 h
(Figs. 4c and d).



255

Figure 4: Maximum reflectivity (dBZ) for WDM6_FD and WDM6_PD are shown in (a) and (b) with the Hovmöller plots of the surface rainfall rate for (c) WDM6_FD and (d) WDM6_PD. The contour interval is 1 mm/10 min for rates of 0–4 mm/10 min, and 3 mm/10 min for the rates greater than 4 mm/10 min in (c) and (d). The grey regions represent the stratiform rain region receiving precipitation at rates of 0.05–4 mm/10 min.



260

The vertical distributions of the time-domain-averaged mixing ratio of hydrometeors for WDM6_FD and WDM6_PD and the differences between the simulations are presented in Fig. 5. The sum of the mixing ratios of snow and graupel is indicated by the red line. The mixing ratio of rain increases below the 6 km level, while that of cloud water decreases over the 4–9 km levels in WDM6_PD (Fig. 5c). Additionally, compared to WDM6_FD, WDM6_PD produces a higher snow mixing ratio above the 3 km level and a lower graupel mixing ratio over the entire layers. Furthermore, in WDM6_PD, the total mixing ratio of snow and graupel is lower below the 7 km level and higher above that level (Fig. 5c). Compared to the results of WDM6_FD, the generation of solid-phase hydrometeors is less effective in the lower layers and more effective in the upper layers in WDM6_PD. Meanwhile, the cloud ice mixing ratio does not show any remarkable difference between WDM6_FD and WDM6_PD.

265

Figure 5: Vertical profiles for the time-domain-averaged mixing ratios (g kg^{-1}) of hydrometeors for (a) WDM6_FD and (b) WDM6_PD. In (a) and (b), the cloud ice mixing ratio (q_I) is multiplied by 10. The difference between the mixing ratios (g kg^{-1}) of WDM6_PD and WDM6_FD (WDM6_PD minus WDM6_FD) is plotted in (c).

270

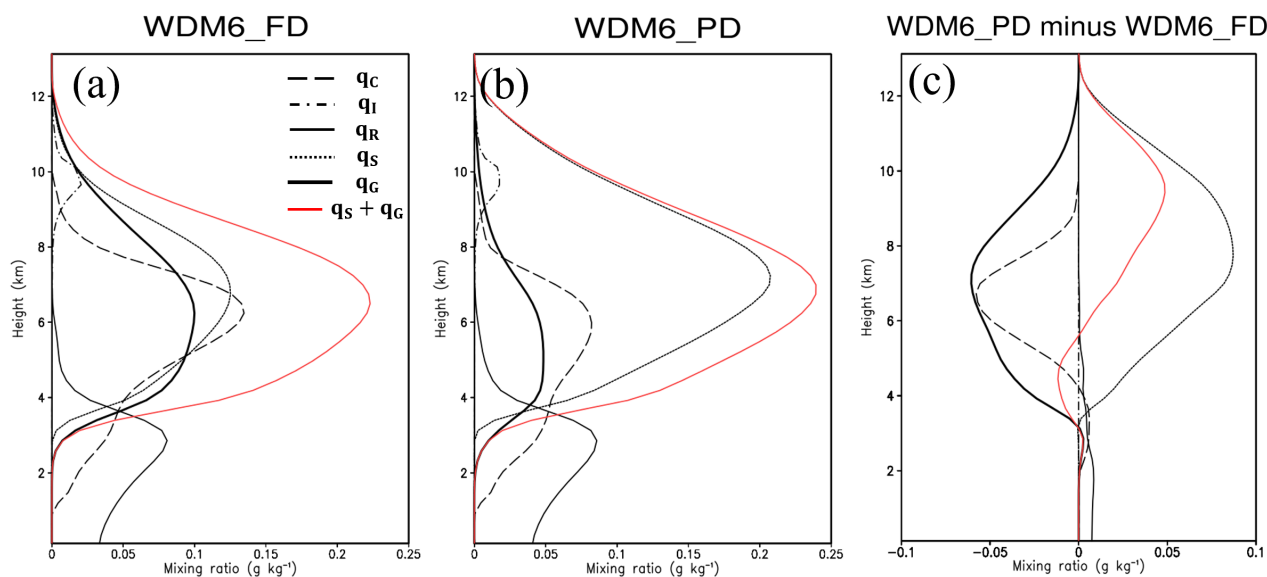


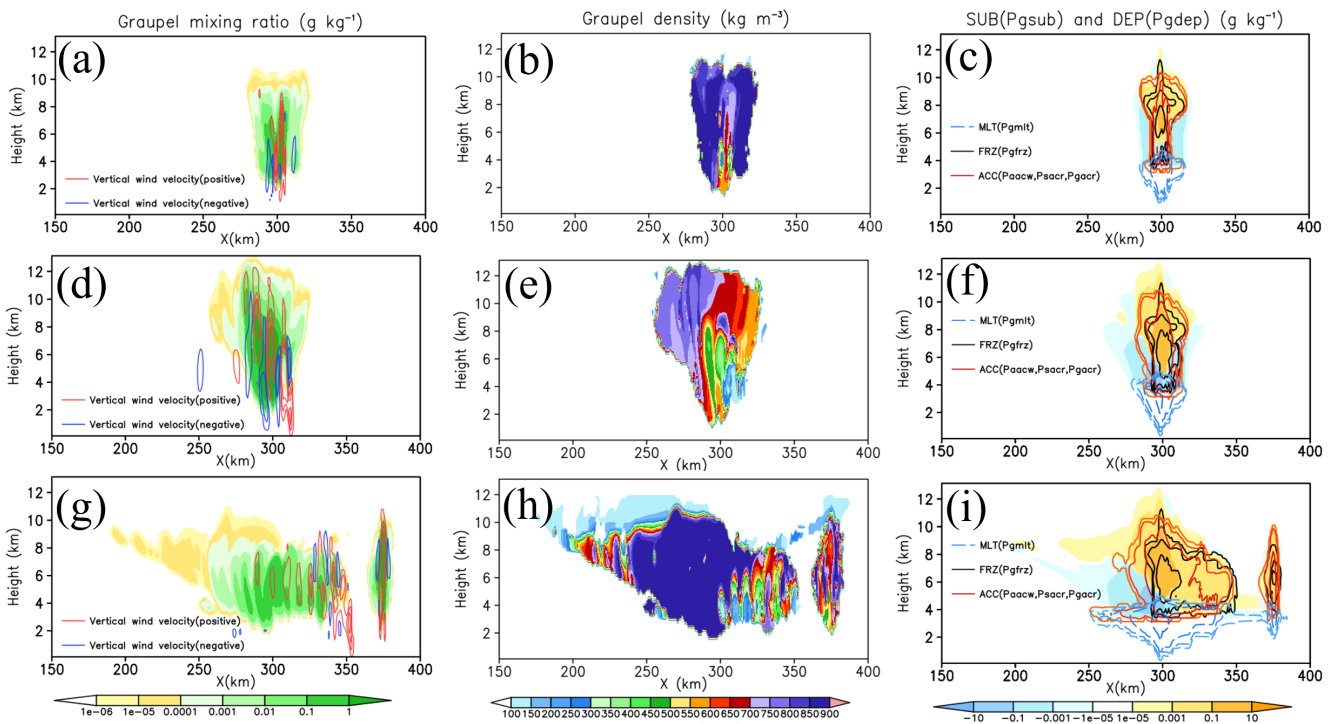
Figure 6 shows the spatial distributions of q_G and ρ_G , with the major source/sink microphysics processes of q_G in WDM6_PD at 1 h (Fig. 6a–c), 2 h (Fig. 6d–f) and 4 h (Fig. 6g–i). Note that ρ_G in WDM6_FD is pre-defined as 500 kg m^{-3} .
 275 During the early development stage of convections, at 1 h, a graupel mixing ratio with relatively low density is generated over the strong updraft region, and some of the particles are transported to the upper level of 11 km (Figs. 6a and b). The microphysical budget analysis shows that particles mostly grow by vapor deposition in the initial stage (Fig. 6c). The sensitivities in ice-phase particle growth and transport due to variabilities in the riming processes over an orographic barrier were examined by using a unique Lagrangian particle-based precipitation model in the study by DeLaFrance et al. (2023). This study revealed that particles initially grow by deposition and have a lower effective density. Very dense graupel (ρ_G values of 900 kg m^{-3}) are located in the marginal regions of updraft cores (Fig. 6b). The main source processes contributing to the graupel mixing ratio are deposition (DEP), accretion (ACC) and freezing (FRZ), and the main sink processes are sublimation (SUB) and melting (MLT), as seen in Fig. 6c. Major ACC processes include the accretion process between cloud water and snow or graupel, that between rain and graupel, and that between rain and snow. At 2 h, graupel continues to be generated through DEP, ACC and FRZ, with a relatively low density of $550\text{--}800 \text{ kg m}^{-3}$ compared to the density in the initial stage (Fig. 6b, c, e and f). The higher values of the graupel mixing ratios are concentrated along the updraft core, resulting in a relatively lower ρ_G (Fig. 6d and e). At 4 h, graupel with a relative lower ρ_G , which can be considered as aggregation-like particles, is transported into anvil cloud region. Over the corresponding region, DEP is the main process producing graupel.

290 **Figure 6: Spatial distribution of q_G (g kg^{-1}) (left column), ρ_G (kg m^{-3}) (middle column) and the major source/sink microphysics processes ($\text{g kg}^{-1} \text{ s}^{-1}$) related to q_G (right column) in WDM6_PD at 1 h (a–c), 2 h (d–f) and 4 h (g–i). In (a), (d) and (g), the solid**



295

red (blue) line represents positive (negative) vertical wind velocity (m s^{-1}). Contour lines for positive (negative) values are at 2, 5 and 8 (–2 and –5) mm. In (c), (f) and (i), the main source processes, namely, deposition (Pgdep ; DEP), accretion (mean of Paacw , Psacr and Pgaer ; ACC) and freezing (Pgrfz ; FRZ) are plotted with the major sink processes, namely, sublimation (Pgsub ; SUB) and melting (Pgmlt ; MLT). Red (blue) colours represent DEP (SUB). The processes of FRZ, ACC and MLT are indicated by solid black, solid red and blue dashed lines, respectively. The contour lines for ACC and FRZ (MLT) values are at $1\text{e-}5$, 0.001, 0.01 and 10 ($-1\text{e-}5$, -0.001 , -0.01 and -10) ($\text{g kg}^{-1} \text{ s}^{-1}$). Detailed descriptions of the microphysical processes are provided in Table 1.



300 4.2 Snowfall experiments

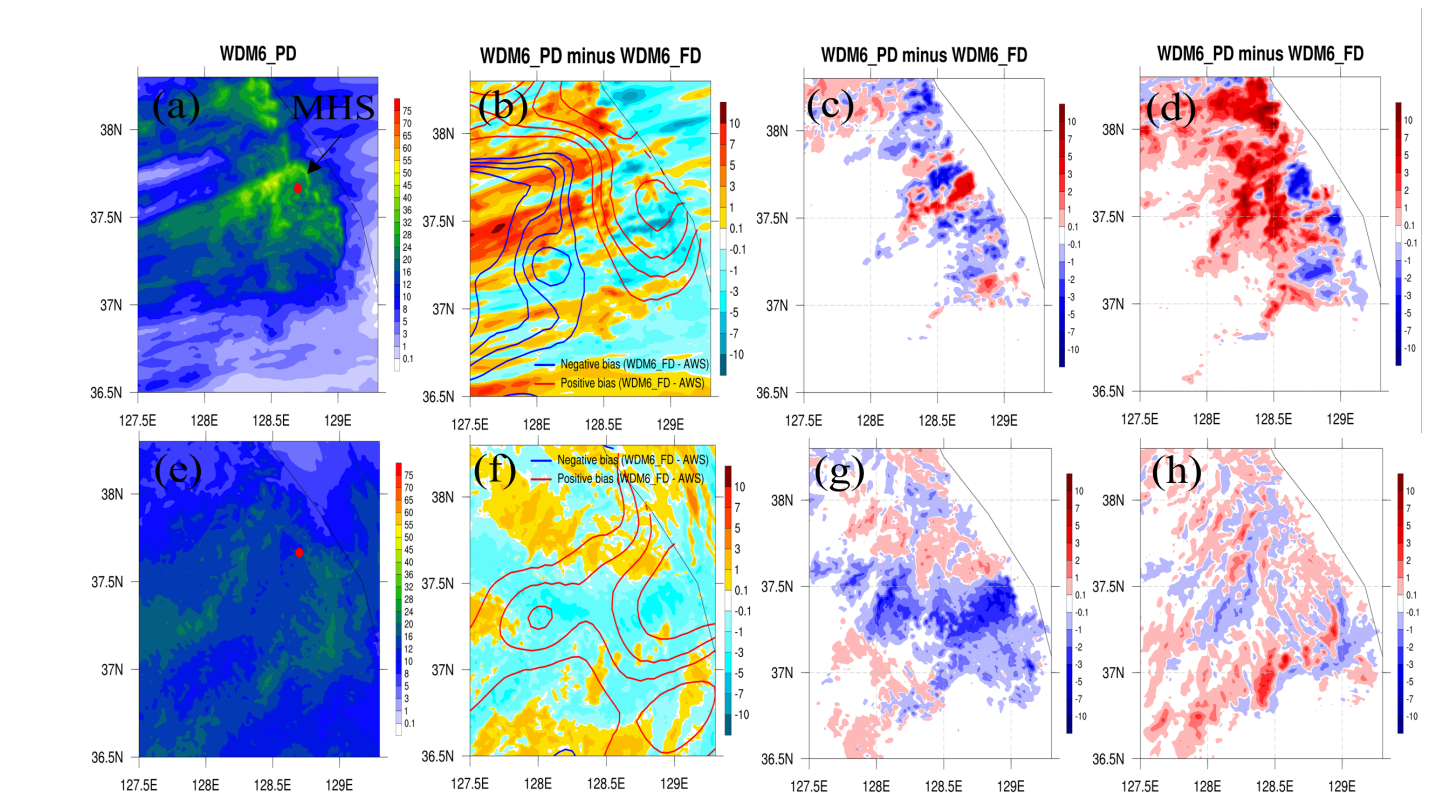
Figure 7 shows the simulated surface precipitation in WDM6_FD and WDM6_PD. In the CL case, most of the simulated rainfall in WDM6_PD is concentrated over the central part of the Korean Peninsula, similar to the AWS observations (Figs. 2a and 7a). WDM6_FD and WDM6_PD provide similar simulated ratios of surface snow and graupel for the CL case. Compared to WDM6_FD, WDM6_PD simulates less precipitation along the coast and mountainous region and more precipitation over the western part of the analysis domain (as indicated by the shading in Fig. 7b). This results in a precipitation spatial distribution that is more comparable to the observed precipitation distribution. WDM6_PD reduces the surface snow amount over the mountainous region and increases the amount of surface graupel over regions with abundant precipitation,

305



relative to WDM6_FD (Figs. 7c and d). These changes in WDM6_PD alleviate the precipitation deficiency in WDM6_FD.
310 Although the bias score for the CL case (Case 1) deteriorates in WDM6_PD, the root mean square error (RMSE) score for all
CL cases (Cases 1 and 3) is much improved (Table 4). In the WL case, the amount of surface snow exceeds that of the surface
graupele; WDM6_PD effectively alleviates the positive bias of surface precipitation, which occurs in WDM6_FD, over most
of the domain (Fig. 7f). Surface snow decreases significantly in WDM6_PD, compared to WDM6_FD, while the surface
graupele increases slightly (Figs. 7g and h). The reduction in surface precipitation amount in WDM6_PD results in an
315 improvement in the RMSE scores for all WL cases, as well as biases for all WL cases except for Case5 (Table 4). Overall, the
equitable threat score (ETS) scores between two experiments are quite similar.

Figure 7: Accumulated surface precipitation amount (mm) for (a) CL and (e) WL cases with WDM6_PD during the analysis period. The differences in the amounts of surface precipitation (mm) between WDM6_PD and WDM6_FD (WDM6_PD minus WDM6_FD) for CL and WL cases are shaded in (b) and (f). The red (blue) solid lines represent the positive (negative) differences between WDM6_FD and AWS observations (WDM6_FD minus AWS). The contour lines for positive (negative) values are plotted at 3, 5, 7 and 10 (−3, −5, −7 and −10) mm. The differences in the amounts of surface snow (mm) between WDM6_PD and WDM6_FD (WDM6_PD minus WDM6_FD) for CL and WL cases are plotted in (c) and (g). The differences in the amounts of surface graupele (mm) are shown in (d) and (h).



325



Table 4. Statistical skill scores of the root mean square error (RMSE) (mm), bias (mm) and equitable threat score (ETS) for different cases with WDM6_FD and WDM6_PD.

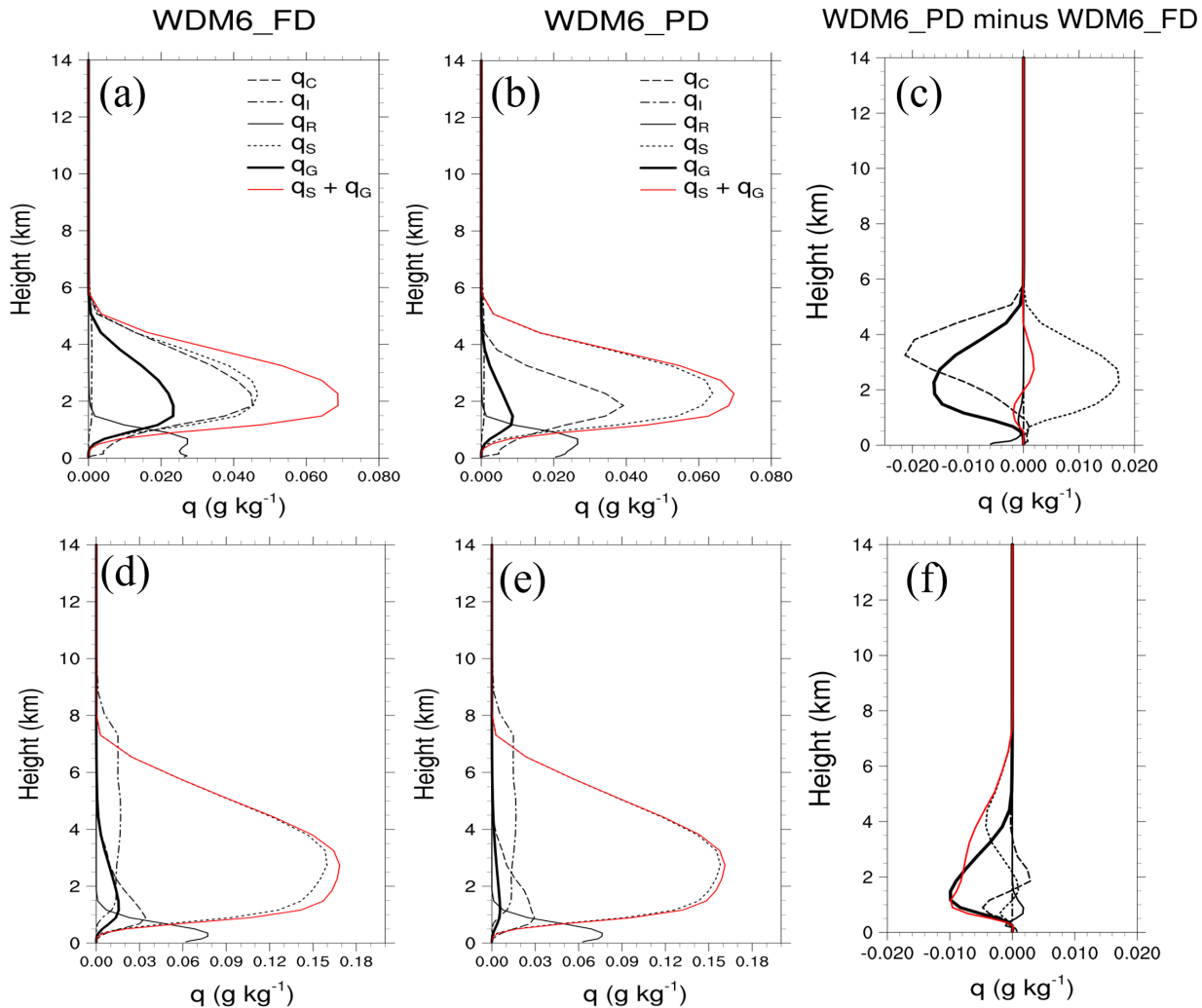
Case	Experiment	RMSE (mm)	BIAS (mm)	ETS
Case1	WDM6_FD	6.58	1.27	0.30
	WDM6_PD	6.01	1.61	0.31
Case2	WDM6_FD	5.49	5.03	0.16
	WDM6_PD	4.36	3.56	0.17
Case3	WDM6_FD	1.81	1.31	0.19
	WDM6_PD	1.63	1.26	0.18
Case4	WDM6_FD	9.51	2.83	0.07
	WDM6_PD	9.00	0.63	0.06
Case5	WDM6_FD	13.95	12.69	0.14
	WDM6_PD	13.79	13.27	0.12
Case6	WDM6_FD	3.94	2.87	0.10
	WDM6_PD	3.55	1.31	0.07
Case7	WDM6_FD	1.67	-1.47	0.10
	WDM6_PD	1.62	-1.36	0.11
Case8	WDM6_FD	2.63	1.20	0.17
	WDM6_PD	1.87	-0.36	0.20

330 The vertical distributions of the time-domain-averaged mixing ratios for WDM6_FD and WDM6_PD are shown in
 Fig. 8. In the CL case, the simulated mixing ratios for all hydrometeors are pronounced below the 6 km level (Figs. 8a and b),
 while in the WL case, hydrometeors are simulated up to the 10 km level (Figs. 8d and e). This is because the WL case comprises
 deeper systems than the CL case. The relative proportion of graupel to the total hydrometeors is greater in the CL case than in
 the WL case. Additionally, for the CL case, the graupel mixing ratio decreases, and the snow mixing ratio increases in
 335 WDM6_PD than in WDM6_FD. Therefore, the total mixing ratio of snow and graupel increases above the 2 km level, while
 it decreases below the level in WDM6_PD relative to WDM6_FD in the CL case, as seen in the 2D idealized case. In
 WDM6_PD, the overall cloud water mixing ratio decreases, and the rain mixing ratio slightly decreases near the surface (Fig.
 8c). The change in graupel mixing ratio in the WL case is similar to those in the CL case (Fig. 8f). The graupel mixing ratio
 decreases significantly below the 5 km level in WDM6_PD. The snow mixing ratio also decreases throughout the layers except



340 at the 1–2 km level, resulting in a smaller total mixing ratio of snow and graupel in WDM6_PD compared to WDM6_FD (Fig. 8f). Meanwhile, the rain, cloud water, and cloud ice mixing ratios of WDM6_FD and WDM6_PD differ only slightly. A noteworthy characteristic of WDM6_PD is the reduction in the graupel mixing ratio over the whole layers regardless of simulation cases, resulting in an increase in the amount of surface graupel deposited (Figs. 7d and h).

345 **Figure 8: Vertical profiles for the time-domain-averaged mixing ratios (g kg^{-1}) of hydrometeors for (a) CL and (d) WL cases with WDM6_FD. (b) and (e) are same as (a) and (d), but for WDM6_PD. The differences in the mixing ratios of WDM6_PD and WDM6_FD (WDM6_PD minus WDM6_FD) for CL and WL cases are plotted in (c) and (f). In (a), (b), (d) and (e), the cloud ice mixing ratio (q_I) is multiplied by 100. The sum of snow and graupel mixing ratios (g kg^{-1}) is indicated by red lines.**

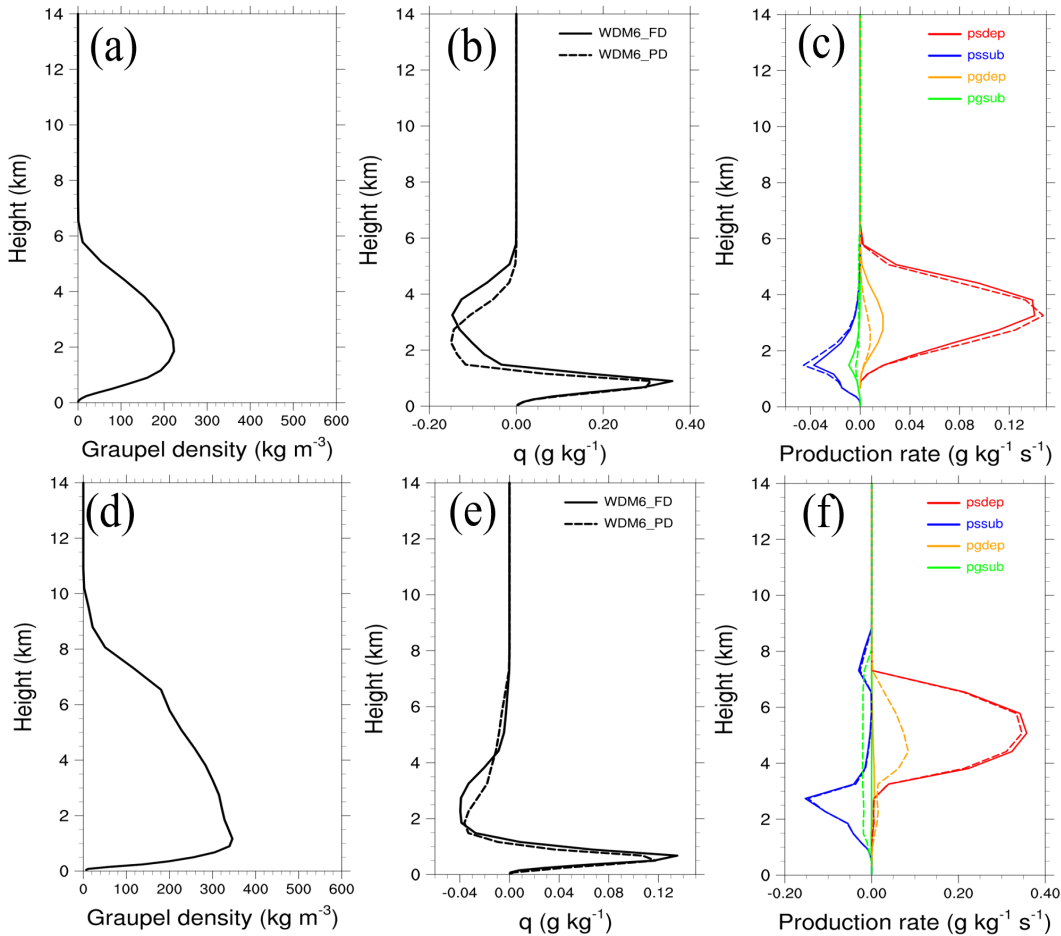




350 The vertical profiles for the time-domain-averaged ρ_G for CL and WL cases are compared in Fig. 9. As shown in Fig.
8, convective cells develop more extensively in the WL case than in the CL case. In the presence of graupel, the time-domain-
averaged ρ_G is simulated up to a higher level in the WL case than in the CL case (Figs. 9a and d). The value of ρ_G is taken as
500 kg m⁻³ in WDM6_FD, whereas it has relatively smaller values of up to 250 and 350 kg m⁻³ in WDM6_PD for the CL and
WL cases, respectively. In WDM6_PD, the time-domain-averaged mass-weighted mean diameter (D_m) is simulated as 0.110
355 and 0.191 mm for the CL and WL cases, respectively, whereas in WDM6_FD, it is simulated as 0.133 (CL) and 0.199 (WL)
mm, indicating that WDM6_PD simulates smaller graupel diameters. Despite smaller values of ρ_G and D_m in WDM6_PD
compared to WDM6_FD, the former simulates a higher graupel fall velocity when considering the simulated D_m in both
simulations (see Fig. 1), leading to more surface graupel in WDM6_PD for CL and WL cases (Figs. 7d and h).

In the CL case, WDM6_PD simulates ρ_G with a maximum value of 220 kg m⁻³ at the 2 km level (Fig. 9a). The
360 maximum level of falling graupel is simulated at a lower altitude of 2 km in the WDM6_PD compared to WDM6_FD, in
which the maximum level is located at 3.5 km (Fig. 9b). As graupel fall quickly in WDM6_PD, graupel deposition (P_{gdep})
decreases, leading to the suppression of graupel generation and sublimation (P_{gsub}) (Fig. 9c). Meanwhile, the deposition of
snow (P_{sdep}) in WDM6_PD, the red lines in Fig. 9c, increases below the 3.5 km level owing to the surplus water vapor relative
to WDM6_FD, leading to an increase in the snow mixing ratio in the atmosphere (Fig. 8c). In the WL case, ρ_G increases
365 significantly up to a value of 350 kg m⁻³ at 1 km level (Fig. 9d). Graupel, which exists up to the 10 km level, fall from a
relatively higher level of 8 km in WDM6_PD than in WDM6_FD (Fig. 9e). The maximum amount of falling graupel is
simulated at a relatively lower level of 1.8 km in WDM6_PD than in WDM6_FD, as seen in the CL case. P_{gdep} efficiently
occurs at a higher level in WDM6_PD than in WDM6_FD (Fig. 9f) possibly because the former simulates more graupel with
a steep increase in ρ_G between the 5 km and 8 km levels. The increase in P_{gdep} in WDM6_PD leads to a reduction in the
370 available water vapor, in turn, causing a reduction in the P_{sdep} and snow mixing ratio values in the atmosphere.

**Figure 9: Vertical profiles for the time-domain-averaged ρ_G (kg m⁻³) for (a) CL and (d) WL cases with WDM6_PD. Time-domain-
averaged falling graupel mixing ratios (g kg⁻¹) depending on the mass-weighted terminal velocity with WDM6_PD and WDM6_FD
for CL and WL cases are in (b) and (e). The solid and dashed lines represent WDM6_FD and WDM6_PD. (c) and (f) show the
375 vertical profiles of time-domain-averaged deposition/sublimation of graupel and snow (g kg⁻¹ s⁻¹) for the CL and WL cases. The
 P_{sdep} , P_{ssub} , P_{gdep} and P_{gsub} are indicated by red, blue, orange and green solid lines, respectively. In (f), P_{gdep} and P_{gsub} are
multiplied by 10.**

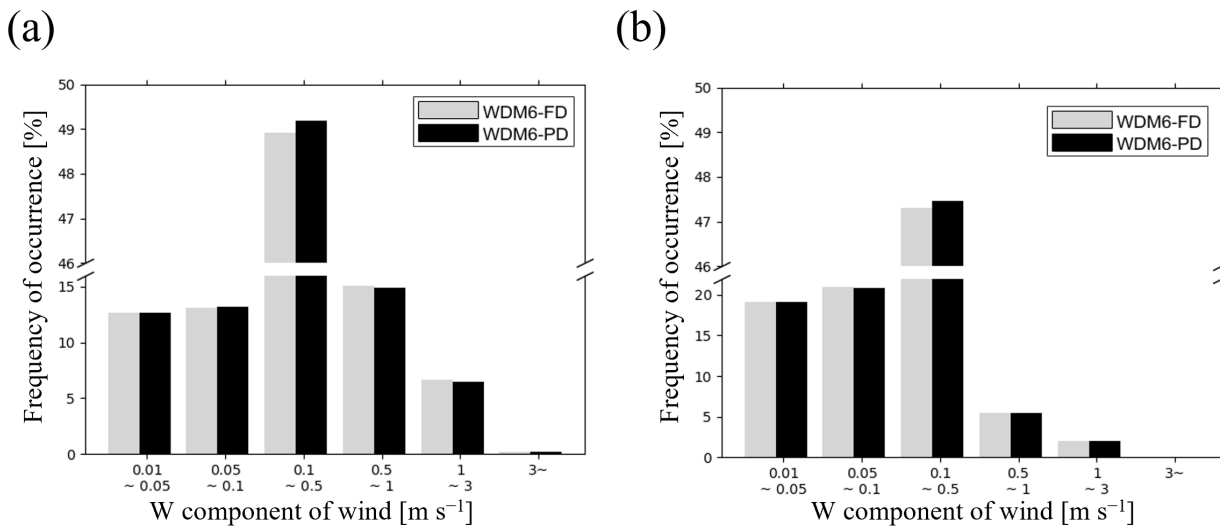


The significantly enhanced graupel fall velocity, attributed to the prognostic graupel density in WDM6_PD, accelerates the sedimentation of graupel. This, in turn, increases the surface graupel amount while decreasing the graupel mixing ratio in the atmosphere. In the CL case, WDM6_PD simulates an enhanced upward motion, especially in the range of $0.1\text{--}0.5 \text{ m s}^{-1}$, compared to WDM6_FD, as shown in Figure 10a. The stronger upward motion in WDM6_PD leads to a portion of snow remaining suspended in the atmosphere without falling to the surface in the CL case. Some studies have demonstrated that the increase in graupel fall velocity induces changes in dynamical and thermodynamic fields, as observed in the CL case of our study. For instance, Adams-Selin et al. (2013) found that faster graupel fall velocities concentrate cooling closer to the convective line by limiting advection, resulting in the formation of an intense cold pool and faster bowing development. Meanwhile, both experiments in the WL case shows a reduction in the strength of upward motion compared to that in the CL case, as shown in Figures 10a and b. In the WL case, WDM6_PD exhibits a reduction in the snow mixing ratio generation because of more inefficient Ps_{dep} , leading to a decrease in the surface snow amount (Figs. 7g and 9f). Figure 10b illustrates



390 that WDM6_PD exhibits a slight enhancement of vertical velocity in the range of 0.1–0.5 m s⁻¹, compared to WDM6_FD, but
 the increase is not as significant as in the CL case.

395 **Figure 10: Frequency of occurrence (%) of the positive vertical component (m s⁻¹) with WDM6_PD and WDM6_FD for the (a) CL
 and (b) WL cases. Gray and black bars represent the WDM6_FD and WDM6_PD, respectively. The model-simulated W is extracted
 from all grid points across the analysis domain at every hour during the analysis period.**

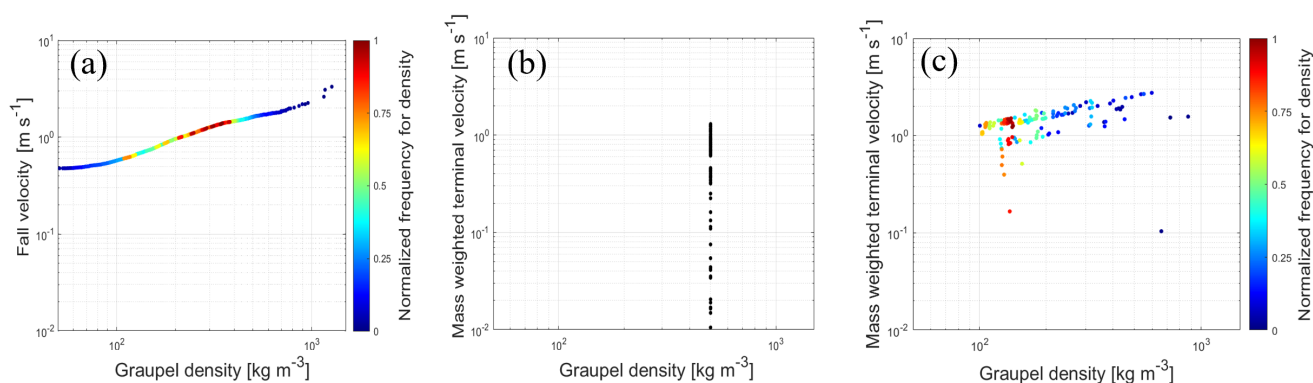


The ρ_G – V_G relationships obtained from the 2DVD measurement at the MHS site, as well as those simulated from
 WDM6_PD and WDM6_FD, are shown in Fig. 11. The observed ρ_G values are in the range of 43.6–1267 kg m⁻³ (Fig. 11a).
 The maximum normalized frequency of the observed ρ_G is shown in the range of approximately 300–400 kg m⁻³, with the
 frequent normalized frequency of ρ_G values between 100 and 400 kg m⁻³. WDM6_FD only presents a single value of ρ_G (500
 kg m⁻³; Fig. 11b), as it is treated as the fixed value in the model and shows a much lower range of graupel fall velocity than
 the observed value. Meanwhile, in WDM6_PD, the range of ρ_G is simulated from 100 to 900 kg m⁻³, as our study sets the
 possible range of ρ_G within this range. WDM6_PD presents the majority of simulated ρ_G at relatively lower values of 150 kg
 m⁻³ compared to the observed value (Figs. 11a and 11c). The fall velocity of graupel, varying with ρ_G , shows a relatively larger
 value in WDM6_PD than in the observations. Although WDM6_PD simulates larger ranges of fall velocity and lower ranges
 of ρ_G , it is closer to the observations than WDM6_FD.

**Figure 11: ρ_G – V_G relationships are shown: (a) 2DVD measurement, (b) WDM6_FD and (c) WDM6_PD. Colour bars in (a) and (b)
 represent the normalized frequency of ρ_G . In (a), graupel particle characteristics measured at the MHS site during the analysis**



410 period of Case 6 are used. For (b) WDM6_PD and (c) WDM6_FD, model-simulated graupel characteristics are extracted over 16-
grid points centred at the MHS site during the analysis period for Cases 2 and 6.



5. Summary and conclusion

415

This study introduces a method to predict graupel density and incorporates the predicted graupel density into the WDM6 microphysics scheme (Park and Lim, 2023). By using the new prognostic variable (graupel volume mixing ratio), graupel density can be prognosed based on the ratio of graupel mixing ratio and its volume mixing ratio, following the study of Milbrandt and Morrison (2013). Therefore, the mass–diameter and fall velocity–diameter relationships of graupel are updated with varying graupel density. To assess the impact of prognostic graupel density on the simulated precipitation system, numerical simulations are conducted for 2D idealized squall line and winter snowfall cases during the ICE-POP 2018 field campaign using the WRF model version 4.1.3. The modified WDM6 requires 22.8% more computational time, considering only cloud microphysical processes, compared to the original WDM6.

420

In the idealized 2D squall line framework, simulations using the original WDM6 and modified WDM6 yield similar surface rain rates associated with squall line development. However, compared to the original WDM6, the modified WDM6 gives higher maximum reflectivity in both the convective cores and the stratiform regions. A comparison of the vertical profiles of the mixing ratios with the modified and original WDM6 confirms a significant decrease in the graupel mixing ratio and an increase in the snow mixing ratio throughout the vertical layers. The vertical cross sections of graupel fields over time reveal that the modified WDM6 can represent a range of graupel densities, from low to high at varying times and in different spaces.

430 For graupel mixing ratio, the main source processes are analyzed as deposition, accretion, and freezing, while the sink processes as sublimation and melting throughout the squall line evolutions.

425

For the winter snowfall cases during the ICE-POP 2018 field campaign, the original WDM6 exhibits a positive bias by simulating more precipitation along the coastal and mountainous regions, irrespective of the specific case. In a shallow system, classified as a CL case in our study, the modified WDM6 provides a better RMSE score than the original WDM6 by



435 reducing surface precipitation over the regions representing positive bias and enhancing it over the western part of the analysis domain. Although the maximum density of graupel in the modified WDM6 is smaller than that in the original WDM6, the fall velocity of graupel is greater in the modified WDM6 because of the newly employed graupel fall velocity relationship. Faster sedimentation of graupel leads to inefficient graupel deposition. This, in turn, results in a decrease in the graupel mixing ratio and presence of more snow suspended in the atmosphere. The increased snow is a result of efficient snow deposition with surplus water vapor. Because of the enhanced upward motion of the convection systems in the modified WDM6 results, snow remains suspended in the atmosphere instead of falling to the surface. Therefore, a decrease in surface snow over the mountainous region and an increase in surface graupel over regions with abundant precipitation mitigate the surface precipitation deficiency in the original WDM6.

445 In the deep system, classified as a WL case, the modified WDM6 reduces surface snow to mitigate the excessive precipitation bias observed in the original WDM6 simulation over the entire domain. In this case, the surface amounts of snow exceed those of graupel, unlike in a CL case where the simulated amounts of surface snow and graupel are similar. Therefore, the change in surface snow is mainly attributed to changes in the surface precipitation. A greater graupel deposition in the 4–8 km level in the modified WDM6 consumes more water vapor, leading to inefficient snow deposition in the corresponding level. Hence, the snow mixing ratio in the atmosphere and at the surface decreases in the modified WDM6, leading to improved RMSE scores in all WL cases than in the original WDM6. Both experiments in a WL case show a reduction in the strength of upward motion relative to those in a CL case.

455 The simulated fall velocity–density relationship of graupel is verified using 2DVD measurement data for a WL snowfall case that occurred during the ICE-POP 2018 field campaign. Although the modified WDM6 simulates slightly larger ranges of fall velocity and lower ranges of graupel density, it captures the observed relationship between graupel density and fall velocity fairly well. In contrast, the original WDM6, with a fixed graupel density, not only underestimates the graupel fall velocities but also predicts a wider range of fall velocity compared to the observed values. It is worth noting that our study is distinguished by its attempt to compare simulated graupel characteristics with observed data during ICE-POP 2018. The co-located MASC measurements, coupled with the 2DVD measurement, enhance the quality of graupel identification in our research. The V_G – D_G relationship in the modified WDM6 is derived using the least-squares method in a log–log space at the given graupel density; therefore, there is room to further refine the simulated fall velocity.

Code and data availability. The WRF model version 4.1.3 is available at <https://github.com/wrf-model/WRF/releases> (last access: January 2022). The ERA-Interim reanalysis data from the European Centre for Medium-Range Weather Forecasts (ECMWF) for initial and boundary conditions is available at <https://apps.ecmwf.int/datasets/data/interim-full-daily/levtype=pl/> and <https://apps.ecmwf.int/datasets/data/interim-full-daily/levtype=sfc/> (last access: October 2019). The model codes, model output, and scripts and that cover every data and figure processing action for all the results reported in this paper are available at <https://doi.org/10.5281/zenodo.10074701>. The 2DVD data are available at



https://doi.org/10.5281/zenodo.10126522. Model output is available upon the request (Sun-Young Park at ililpo1107@gmail.com).

470 **Author contributions.** SP designed and performed the model simulations and analysis under the supervision of KL. KL and SP wrote the manuscript with substantial contributions from all co-authors. KK processed the observational data. JAM provided the code to predict the prognostic volume mixing ratio of graupel. KL, GL, and JAM contributed to the scientific discussions and gave constructive advice.

Competing interests. The authors declare that they have no conflict of interest.

475 **Special issue statement.** This article is part of the special issue “Winter weather research in complex terrain during ICE-POP 2018 (International Collaborative Experiments for PyeongChang 2018 Olympic and Paralympic winter games) (ACP/AMT/GMD inter-journal SI)”. It is not associated with a conference.

Funding. This work was supported by the National Research Foundation of Korea (NRF) grant funded by the Korean government (MSIT) (RS-2023-00208394).

480 **Acknowledgments.** The authors are greatly appreciative to the participants of the World Weather Research Program Research Development Project and Forecast Demonstration Project, International Collaborative Experiments for Pyeongchang 2018 Olympic and Paralympic winter games (ICE-POP 2018), hosted by the Korea Meteorological Administration.

References

- Adams-Selin, R. D., van den Heever, S. C. and Johnson, R. H.: Impact of Graupel Parameterization Schemes on Idealized
485 Bow Echo Simulations, *Mon. Wea. Rev.*, 141, 1241–1262, <https://doi.org/10.1175/MWR-D-12-00064.1>, 2013.
- Bae, S. Y., Hong, S. Y., and Tao, W. K.: Development of a single-moment cloud microphysics scheme with prognostic hail for the Weather Research and Forecasting (WRF) model, *Asia-Pacific J. Atmos. Sci.*, 55, 233-245, <https://doi.org/10.1007/s13143-018-0066-3>, 2019.
- Böhm, H. P.: A General Equation for the Terminal Fall Speed of Solid Hydrometeors, *J. Atmos. Sci.*, 46, 2419-2427,
490 [https://doi.org/10.1175/1520-0469\(1989\)046<2419:AGEFTT>2.0.CO;2](https://doi.org/10.1175/1520-0469(1989)046<2419:AGEFTT>2.0.CO;2), 1989.
- Bryan, G. H., and Morrison, H.: Sensitivity of a Simulated Squall Line to Horizontal Resolution and Parameterization of Microphysics, *Mon. Wea. Rev.*, 140, 202-225, <https://doi.org/10.1175/MWR-D-11-00046.1>, 2012.
- Chen, F., and Dudhia, J.: Coupling an advanced land surface-hydrology model with the Penn State-NCAR MM5 modeling system. Part I: Model implementation and sensitivity, *Mon. Weather Rev.*, 129, 569-585, [https://doi.org/10.1175/1520-0493\(2001\)129<0569:CAALSH>2.0.CO;2](https://doi.org/10.1175/1520-0493(2001)129<0569:CAALSH>2.0.CO;2), 2001.
495



- Cohen, C., and McCaul, E. W.: The Sensitivity of Simulated Convective Storms to Variations in Prescribed Single-Moment Microphysics Parameters that Describe Particle Distributions, Sizes, and Numbers, *Mon. Wea. Rev.*, 134, 2547-2565, <https://doi.org/10.1175/MWR3195.1>, 2006.
- 500 Comin, A. N., Schumacher, V., Justino, F., and Fernández, A.: Impact of different microphysical parameterizations on extreme snowfall events in the Southern Andes. *Weather, Clim. Extrem.*, 21, 65-75, <https://doi.org/10.1016/j.wace.2018.07.001>, 2018.
- Cotton, W. R., Tripoli, G. J., Rauber, R. M., and Mulvihill, E. A.: Numerical simulation of the effects of varying ice crystal nucleation rates and aggregation processes on orographic snowfall, *J. Clim. Appl. Meteorol.*, 25, 1658-1680, [https://doi.org/10.1175/1520-0450\(1986\)025<1658:NSOTEO>2.0.CO;2](https://doi.org/10.1175/1520-0450(1986)025<1658:NSOTEO>2.0.CO;2), 1986.
- 505 Dawson, D. T., Mansell, E. R., Jung, Y., L. Wicker, J., Kumjian, M. R., and Xue, M.: Low-Level ZDR Signatures in Supercell Forward Flanks: The Role of Size Sorting and Melting of Hail, *J. Atmos. Sci.*, 71, 276-299, <https://doi.org/10.1175/JAS-D-13-0118.1>, 2014.
- Dee, D. P., and coauthors: The ERA-Interim reanalysis: configuration and performance of the data assimilation system, *Q. J. R. Meteorol. Soc.*, 137, 553-597, <https://doi.org/10.1002/qj.828>, 2011a.
- 510 DeLaFrance, A., McMurdie, L. A., Rowe, A. K., and Conrick, R.: Effects of Riming on Ice-Phase Precipitation Growth and Transport Over an Orographic Barrier, *Adv. Model. Earth Syst.*, under review, 2023.
- Ferrier, B. S.: A Double-Moment Multiple-Phase Four-Class Bulk Ice Scheme. Part I: Description, *J. Atmos. Sci.*, 51, 249-280, [https://doi.org/10.1175/1520-0469\(1994\)051<0249:ADMMPF>2.0.CO;2](https://doi.org/10.1175/1520-0469(1994)051<0249:ADMMPF>2.0.CO;2), 1994.
- Geresdi, I.: Idealized simulation of the Colorado hailstorm case: Comparison of bulk and detailed microphysics. *Atmos. Res.*, 45(4), 237-252, [https://doi.org/10.1016/S0169-8095\(97\)00079-3](https://doi.org/10.1016/S0169-8095(97)00079-3), 1998.
- 515 Gilmore, M. S., Straka, J. M., and Rasmussen, E. N.: Precipitation Uncertainty Due to Variations in Precipitation Particle Parameters within a Simple Microphysics Scheme, *Mon. Wea. Rev.*, 132, 2610-2627, <https://doi.org/10.1175/MWR2810.1>, 2004.
- 520 Grabowski, W. W., Morrison, H., Shima, S.-I., Abade, G. C., Dziekan, P., and Pawlowska, H.: Modeling of cloud microphysics: Can we do better?, *Bulletin of the American Meteorological Society*, 100(4), 655-672. <https://doi.org/10.1175/BAMS-D-18-0005.1>, 2019.
- Hong, S. Y., and Lim, J. O. J.: The WRF single-moment 6-class microphysics scheme (WSM6), *Asia-Pac. J. Atmospheric Sci.*, 42(2), 129-151, 2006.
- Hong, S. Y., Noh, Y., and Dudhia, J.: A new vertical diffusion package with an explicit treatment of entrainment processes, *Mon. Weather Rev.*, 134, 2318-2341, <https://doi.org/10.1175/MWR3199.1>, 2006.
- 525 Huang, G. J., Bringi, V. N., Moisseev, D., Petersen, W. A., Bliven, L., and Hudak, D.: Use of 2D-video disdrometer to derive mean density-size and Ze-SR relations: Four snow cases from the light precipitation validation experiment, *Atmos. Res.*, 153, 34-48, <https://doi.org/10.1016/j.atmosres.2014.07.013>, 2015.



- Iacono, M. J., Delamere, J. S., Mlawer, E. J., Shephard, M. W., Clough, S. A., and Collins, W. D.: Radiative forcing by long-lived greenhouse gases: Calculations with the AER radiative transfer models, *J. Geophys. Res.*, 113, D13103, <https://doi.org/10.1029/2008JD009944>, 2008.
- 530 Jensen, A. A., Harrington, J. Y., Morrison, H., and Milbrandt, J. A.: Predicting Ice Shape Evolution in a Bulk Microphysics Model, *J. Atmos. Sci.*, 74, 2081-2104, <https://doi.org/10.1175/JAS-D-16-0350.1>, 2017.
- Jensen, A. A., Thompson, G., Ikeda, K., and Tessendorf, S. A.: Improving the Representation of Hail in the Thompson Microphysics Scheme, *Mon. Wea. Rev.*, 151, 2307-2332, <https://doi.org/10.1175/MWR-D-21-0319.1>, 2023.
- 535 Jeoung, H., Liu, G., Kim, K., Lee, G., and Seo, E.-K.: Microphysical properties of three types of snow clouds: implication for satellite snowfall retrievals, *Atmos. Chem. Phys.*, 20, 14491-14507, <https://doi.org/10.5194/acp-20-14491-2020>, 2020.
- Jiménez, P. A., Dudhia, J., González-Rouco, J. F., Navarro, J., Montávez, J. P., and García-Bustamante, E.: A revised scheme for the WRF surface layer formulation, *Mon. Weather Rev.*, 140, 898-918, <https://doi.org/10.1175/MWR-D-11-00056.1>, 2012.
- Johnson, M., Jung, Y. D., Dawson, T., and Xue, M.: Comparison of Simulated Polarimetric Signatures in Idealized Supercell Storms Using Two-Moment Bulk Microphysics Schemes in WRF, *Mon. Wea. Rev.*, 144, 971-996, <https://doi.org/10.1175/MWR-D-15-0233.1>, 2016.
- 540 Jouan, C., and Milbrandt, J. A.: The Importance of the Ice-Phase Microphysics Parameterization for Simulating the Effects of Changes to CCN Concentrations in Deep Convection, *J. Atmos. Sci.*, 76, 1727-1752, <https://doi.org/10.1175/JAS-D-18-0168.1>, 2019.
- 545 Kain, J. S.: The Kain-Fritsch convective parameterization: an update, *J. Appl. Meteorol. Climatol.*, 43, 170-181, [https://doi.org/10.1175/1520-0450\(2004\)043<0170:TKCPAU>2.0.CO;2](https://doi.org/10.1175/1520-0450(2004)043<0170:TKCPAU>2.0.CO;2), 2004.
- Khain, A. P., Pokrovsky, A. M., Seifert, A., and Philips, V. Simulation of effects of atmospheric aerosols on deep turbulent convective clouds by using a spectral microphysics mixed-phase cumulus cloud model. Part I: Model description and possible applications, *J. Atmos. Sci.*, 61, 2963-2982, <https://doi.org/10.1175/JAS-3350.1>, 2004a.
- 550 Khvorostyanov, V. I., and Curry, J. A.: Terminal velocities of droplets and crystals: Power laws with continuous parameters over the size spectrum, *J. Atmos. Sci.*, 59, 1872-1884, [https://doi.org/10.1175/1520-0469\(2002\)059<1872:TVODAC>2.0.CO;2](https://doi.org/10.1175/1520-0469(2002)059<1872:TVODAC>2.0.CO;2), 2002.
- Kim, K. B., Lim, K. S. S., and Lee, J.: Numerical Errors in Ice Microphysics Parameterizations and their Effects on Simulated Regional Climate, *Asia-Pacific J. Atmos. Sci.*, 58, 679-695, <https://doi.org/10.1007/s13143-022-00288-z>, 2022.
- 555 Kim, K., Bang, W., Chang, E.-C., Tapiador, F. J., Tsai, C.-L., Jung, E., and Lee, G.: Impact of wind pattern and complex topography on snow microphysics during International Collaborative Experiment for PyeongChang 2018 Olympic and Paralympic winter games (ICE-POP 2018), *Atmos. Chem. Phys.*, 21, 11955-11978, <https://doi.org/10.5194/acp-21-11955-2021>, 2021a.
- Ko, J. S., Lim, K. S. S., Kim, K., Lee, G., Thompson, G., and Berne, A.: Simulated microphysical properties of winter storms from bulk- type microphysics schemes and their evaluation in the Weather Research and Forecasting (v4.1.3) model during the ICE-POP 2018 field campaign, *Geosci. Model Dev.*, 15(11), 4529-4553, <https://doi.org/10.5194/gmd-15-4529-2022>, 2022.
- 560



- Labriola, J., Snook, N., Jung, Y., Putnam, B., and Xue, M.: Ensemble Hail Prediction for the Storms of 10 May 2010 in South-Central Oklahoma Using Single- and Double-Moment Microphysical Schemes, *Mon. Wea. Rev.*, 145, 4911–4936, <https://doi.org/10.1175/MWR-D-17-0039.1>, 2017.
- 565 Lebo, Z. J. and Seinfeld, J. H.: Theoretical basis for convective invigoration due to increased aerosol concentration, *Atmos. Chem. Phys.*, 11, 5407–5429, <https://doi.org/10.5194/acp-11-5407-2011>, 2011.
- Li, J., Ye, Q., Li, F., and Chen, Y.: A cloud-resolving simulation study of monthly-scale autumn precipitation on Hainan Island: The effects of three categories of Graupel on rainfall, *Atmos. Res.*, 220, 92–108, <https://doi.org/10.1016/j.atmosres.2019.01.008>, 2019.
- 570 Lim, K. S. S., Chang, E., Sun, R., Kim, K., Tapiador, F. J., and Lee, G.: Evaluation of simulated winter precipitation using WRF-ARW during the ICE-POP 2018 field campaign. *Wea. Forecasting.*, 35(5), 2199–2213, <https://doi.org/10.1175/WAF-D-19-0236.1>, 2020.
- Lim, K. S., and Hong, S.: Development of an Effective Double-Moment Cloud Microphysics Scheme with Prognostic Cloud Condensation Nuclei (CCN) for Weather and Climate Models, *Mon. Wea. Rev.*, 138, 1587–1612, <https://doi.org/10.1175/2009MWR2968.1>, 2010.
- 575 Lin, Y. L., Farley, R. D., and Orville, H. D.: Bulk Parameterization of the Snow Field in a Cloud Model, *J. Climate Appl. Meteor.*, 22, 1065–1092, [https://doi.org/10.1175/1520-0450\(1983\)022<1065:BPOTSF>2.0.CO;2](https://doi.org/10.1175/1520-0450(1983)022<1065:BPOTSF>2.0.CO;2), 1983.
- Liu, C., Ikeda, K., Thompson, G., Rasmussen, R., and Dudhia, J.: High-Resolution Simulations of Wintertime Precipitation in the Colorado Headwaters Region: Sensitivity to Physics Parameterizations, *Mon. Wea. Rev.*, 139, 3533–3553, <https://doi.org/10.1175/MWR-D-11-00009.1>, 2011.
- 580 Mansell, E. R., Ziegler, C. L., and Bruning, E. C.: Simulated Electrification of a Small Thunderstorm with Two-Moment Bulk Microphysics, *J. Atmos. Sci.*, 67, 171–194, <https://doi.org/10.1175/2009JAS2965.1>, 2010.
- McMillen, J. D., and Steenburgh, W. J.: Impact of microphysics parameterizations on simulations of the 27 October 2010 great Salt Lake- effect snowstorm, *Wea. Forecasting.*, 30(1), 136–152, <https://doi.org/10.1175/WAF-D-14-00060.1>, 2015.
- 585 Meyers, M. P., Walko, R. L., Harrington, J. Y., and Cotton, W. R.: New RAMS cloud microphysics parameterization. Part II: The two-moment scheme, *Atmos. Res.*, 45, 3–39, [https://doi.org/10.1016/S0169-8095\(97\)00018-5](https://doi.org/10.1016/S0169-8095(97)00018-5), 1997.
- Milbrandt, J. A., and Morrison, H.: Prediction of Graupel Density in a Bulk Microphysics Scheme, *J. Atmos. Sci.*, 70, 410–429, <https://doi.org/10.1175/JAS-D-12-0204.1>, 2013.
- Milbrandt, J. A., and Yau, M. K.: A Multimoment Bulk Microphysics Parameterization. Part I: Analysis of the Role of the Spectral Shape Parameter, *J. Atmos. Sci.*, 62, 3051–3064, <https://doi.org/10.1175/JAS3534.1>, 2005.
- 590 Min, K., Choo, S., Lee, D., and Lee, G.: Evaluation of WRF Cloud Microphysics Schemes Using Radar Observations, *Wea. Forecasting.*, 30, 1571–1589, <https://doi.org/10.1175/WAF-D-14-00095.1>, 2015.
- Mitchell, D. L., and Heymsfield, A. J.: The treatment of ice particle terminal velocities, highlighting aggregates, *J. Atmos. Sci.*, 62, 1637–1644, <https://doi.org/10.1175/JAS3413.1>, 2005.



- 595 Mitchell, D. L.: Use of mass- and area-dimensional power laws for determining precipitation particle terminal velocities, *J. Atmos. Sci.*, 53, 1710–1723, [https://doi.org/10.1175/1520-0469\(1996\)053<1710:UOMAAD>2.0.CO;2](https://doi.org/10.1175/1520-0469(1996)053<1710:UOMAAD>2.0.CO;2), 1996.
- Morrison, H., and Grabowski, W. W.: Modeling Supersaturation and Subgrid-Scale Mixing with Two-Moment Bulk Warm Microphysics, *J. Atmos. Sci.*, 65, 792–812, <https://doi.org/10.1175/2007JAS2374.1>, 2008.
- Morrison, H., and Milbrandt, J. A.: Parameterization of Cloud Microphysics Based on the Prediction of Bulk Ice Particle
600 Properties. Part I: Scheme Description and Idealized Tests, *J. Atmos. Sci.*, 72, 287–311, <https://doi.org/10.1175/JAS-D-14-0065.1>, 2015.
- Morrison, H., and Milbrandt, J. A.: Comparison of two-moment bulk microphysics schemes in idealized supercell thunderstorm simulations, *Mon. Wea. Rev.*, 139(4), 1103–1130, <https://doi.org/10.1175/2010MWR3433.1>, 2011.
- Morrison, H., Milbrandt, J. A., Bryan, G. H., Ikeda, K., Tessendorf, S. A., and Thompson, G.: Parameterization of cloud
605 microphysics based on the prediction of bulk ice particle properties. Part II: Case study comparisons with observations and other schemes, *J. Atmos. Sci.*, 72(1), 312–339, <https://doi.org/10.1175/JAS-D-14-0066.1>, 2015.
- Morrison, H., Thompson, G. and Tatarskii, V.: Impact of Cloud Microphysics on the Development of Trailing Stratiform Precipitation in a Simulated Squall Line: Comparison of One- and Two-Moment Schemes, *Mon. Wea. Rev.*, 137, 991–1007, <https://doi.org/10.1175/2008MWR2556.1>, 2009.
- 610 Morrison, H., van Lier-Walqui, M., Fridlind, A. M., Grabowski, W. W., Harrington, J. Y., Hoose, C., et al.: Confronting the challenge of modeling cloud and precipitation microphysics, *Adv. Model. Earth Syst.*, 12(8), e2019MS001689, <https://doi.org/10.1029/2022GL102466>, 2020.
- Park, S. Y., and Lim, K. S. S.: Implementation of Prognostic Cloud Ice Number Concentrations for the Weather Research and Forecasting (WRF) Double-Moment 6-Class (WDM6) Microphysics Scheme, *Adv. Model. Earth Syst.*, 15(2),
615 e2022MS003009, <https://doi.org/10.1029/2022MS003009>, 2023.
- Praz, C., Roulet, Y.-A., and Berne, A.: Solid hydrometeor classification and riming degree estimation from pictures collected with a Multi-Angle Snowflake Camera, *Atmos. Meas. Tech.*, 10, 1335–1357, <https://doi.org/10.5194/amt-10-1335-2017>, 2017.
- Reisin, T., Levin, Z. and Tzivion, S.: Rain Production in Convective Clouds As Simulated in an Axisymmetric Model with
620 Detailed Microphysics. Part I: Description of the Model, *J. Atmos. Sci.*, 53, 497–519, [https://doi.org/10.1175/1520-0469\(1996\)053<0497:RPICCA>2.0.CO;2](https://doi.org/10.1175/1520-0469(1996)053<0497:RPICCA>2.0.CO;2), 1996.
- Reisner, J., Rasmussen, R. M., and Bruintjes, R. T.: Explicit forecasting of supercooled liquid water in winter storms using the MM5 mesoscale model, *Q. J. R. Meteorol. Soc.*, 124(548), 1071–1107, <https://doi.org/10.1002/qj.49712454804>, 1998.
- Rutledge, S. A., and Hobbs, P.: The Mesoscale and Microscale Structure and Organization of Clouds and Precipitation in
625 Midlatitude Cyclones. VIII: A Model for the “Seeder-Feeder” Process in Warm-Frontal Rainbands, *J. Atmos. Sci.*, 40, 1185–1206, [https://doi.org/10.1175/1520-0469\(1983\)040<1185:TMAMSA>2.0.CO;2](https://doi.org/10.1175/1520-0469(1983)040<1185:TMAMSA>2.0.CO;2), 1983.
- Seifert, A., and Beheng, K. D.: A two-moment cloud microphysics parameterization for mixed-phase clouds. Part 1: Model description, *Meteorol. Atmos. Phys.*, 92, 45–66, <https://doi.org/10.1007/s00703-005-0112-4>, 2006a.



- 630 Shima, S. I., Sato, Y., Hashimoto, A., and Misumi, R.: Predicting the morphology of ice particles in deep convection using the super-droplet method: Development and evaluation of SCALE-SDM 0.2. 5-2.2. 0,-2.2. 1, and-2.2. 2., *Geosci. Model Dev.*, 13(9), 4107-4157, <https://doi.org/10.5194/gmd-13-4107-2020>, 2020.
- Skamarock, W. C., and coauthors: A description of the advanced research WRF version 3 (2008) NCAR Technical Note, NCAR, Boulder, CO, 2008.
- Song, H. J., and Sohn, B. J.: An Evaluation of WRF Microphysics Schemes for Simulating the Warm-Type Heavy Rain over the Korean Peninsula, *Asia-Pacific J. Atmos. Sci.*, 54, 225-236, <https://doi.org/10.1007/s13143-018-0006-2>, 2018.
- 635 Straka, J. M., and Mansell, E. R.: A Bulk Microphysics Parameterization with Multiple Ice Precipitation Categories, *J. Appl. Meteor. Climatol.*, 44, 445-466, <https://doi.org/10.1175/JAM2211.1>, 2005.
- Thompson, G., and Eidhammer, T.: A Study of Aerosol Impacts on Clouds and Precipitation Development in a Large Winter Cyclone, *J. Atmos. Sci.*, 71, 3636–3658, <https://doi.org/10.1175/JAS-D-13-0305.1> , 2014.
- 640 Thompson, G., Rasmussen, R. M., and Manning, K.: Explicit Forecasts of Winter Precipitation Using an Improved Bulk Microphysics Scheme. Part I: Description and Sensitivity Analysis, *Mon. Wea. Rev.*, 132, 519-542, [https://doi.org/10.1175/1520-0493\(2004\)132<0519:EFOWPU>2.0.CO;2](https://doi.org/10.1175/1520-0493(2004)132<0519:EFOWPU>2.0.CO;2), 2004.
- Tsai, T., and Chen, J.: Multimoment Ice Bulk Microphysics Scheme with Consideration for Particle Shape and Apparent Density. Part I: Methodology and Idealized Simulation, *J. Atmos. Sci.*, 77, 1821–1850, [https://doi.org/10.1175/JAS-D-19-](https://doi.org/10.1175/JAS-D-19-0125.1)
645 [0125.1](https://doi.org/10.1175/JAS-D-19-0125.1), 2020.
- Wisner, C., Orville, H. D., and Myers, C.: A Numerical Model of a Hail-Bearing Cloud, *J. Atmos. Sci.*, 29, 1160–1181, [https://doi.org/10.1175/1520-0469\(1972\)029<1160:ANMOAH>2.0.CO;2](https://doi.org/10.1175/1520-0469(1972)029<1160:ANMOAH>2.0.CO;2), 1972.